Author/s:
Yan, W;Shresha, VR;Jeangros, Q;Azar, NS;Balendhran, S;Ballif, C;Crozier, K;Bullock, J

Title:
Spectrally Selective Mid-Wave Infrared Detection Using Fabry-Pérot Cavity Enhanced Black Phosphorus 2D Photodiodes.

Date:
2020-10-27

Citation:
Yan, W., Shresha, V. R., Jeangros, Q., Azar, N. S., Balendhran, S., Ballif, C., Crozier, K. & Bullock, J. (2020). Spectrally Selective Mid-Wave Infrared Detection Using Fabry-Pérot Cavity Enhanced Black Phosphorus 2D Photodiodes.. ACS Nano, 14 (10), pp.13645-13651. https://doi.org/10.1021/acsnano.0c05751.

Persistent Link:
https://hdl.handle.net/11343/295017

Spectrally Selective Mid-Wave Infrared Detection Using Fabry-Pérot Cavity Enhanced Black Phosphorus 2D Photodiodes

Wei Yan[1], Vivek Raj Shresha[2,3], Quentin Jeangros[4], Nima Sefidmooye Azar[1], Sivacarendran Balendhran[2], Christophe Ballif[4], Kenneth Crozier[1,2,5], James Bullock[1,]*

[1]Department of Electrical and Electronic Engineering, University of Melbourne, Victoria, Australia. [2]School of Physics, University of Melbourne, Victoria, Australia. [3]Melbourne Centre for Nanofabrication (MCN), Clayton, Victoria, Australia. [4]École Polytechnique Fédérale de Lausanne (EPFL), Institute of Microengineering (IMT), Photovoltaics and Thin-Film Electronics Laboratory (PV-Lab), Neuchâtel, Switzerland. [5]Australian Research Council (ARC) Centre of Excellence for Transformative Meta-Optical Systems (TMOS), University of Melbourne, Victoria, Australia.

[*]Corresponding Author: james.bullock@unimelb.edu.au

ABSTRACT: Thin two-dimensional (2D) material absorbers have the potential to reduce volume dependent thermal noise in infrared detectors. However, any reduction in noise must be balanced against lower absorption from the thin layer, which necessitates advanced optical architectures. Such architectures can be particularly effective for applications that require detection only within a specific narrow wavelength range. This study presents a Fabry-Pérot cavity enhanced bP/MoS_2 mid-wave infrared (MWIR) photodiode. This simple structure enables tunable narrow-band (down to 0.42 μm full-width-half-maximum) photodetection in the 2–4 μm range by adjusting the thickness of the Fabry-Pérot cavity resonator. This is achieved whilst maintaining room temperature performance metrics comparable to previously reported 2D MWIR detectors. Zero bias specific detectivity and responsivity values of 1.7 × 10^9 cm $\mathrm{Hz}^{1/2}$ W^{-1} and 0.11 A W^{-1} at $\lambda = 3.0$ μm are measured, with rise/fall times around 7 μs. These results introduce a promising family of 2D detectors with applications in MWIR spectroscopy.

Keywords: *2D materials, Black phosphorus, Fabry-Pérot cavity, narrow band semiconductors, mid-wave infrared photodiode*

Infrared photodetectors, including those operating in the mid-wave infrared (3–5 μm, MWIR), have a broad potential application space spanning medical, military, communications, and astronomy-based fields.[1] Unfortunately, many commercial applications remain unrealized due to a strong trade-off between sensitivity and cost/miniaturisation for traditional infrared detector technologies.[2] In recent years, two-dimensional (2D) material infrared detectors have been demonstrated as an alternative technology, with a potential for lower thermal noise arising from thinner absorbers.[3] Room temperature detectivities on par with industry dominating technologies such as mercury cadmium telluride, have already been shown.[4-6] The widely accepted pathway to test the extremes of this concept involves reducing the 2D material absorber thickness down to the nm-scale (to reduce thermal noise) whilst maintaining a high level of infrared light collection (to increase the signal). This provides an opportunity for the marriage of 2D materials with advanced optical structures which can maximise light coupling into a thin absorber layer.[7-10]

As shown in **Fig. 1a**, one such optical strategy is to embed a 2D material detector in the center of a Fabry-Pérot (FP) cavity. **Fig. 1b** shows the simulated absorption of a 2D material absorber sandwiched between two symmetrical dielectric layers and two gold mirrors thereby forming a FP cavity. This structure enhances absorption in the 2D layer within the narrow resonance range of the FP cavity.[11-13]The resonant response occurs at wavelengths that are an integer multiple of the effective optical thickness of the cavity. As evident from **Fig. 1b**, the position of the narrow wavelength range can be redshifted, by symmetrically increasing the dielectric thickness surrounding the absorber. This strategy greatly boosts light-matter interaction for nm-scale absorbers, hence it is a perfect combination for 2D materials.[6] The ability to selectively increase absorption in a narrow spectral range also makes this approach useful for spectroscopic applications, such as nondispersive infrared (NDIR) gas sensing.[14] Similar concepts have been explored for 2D materials in the visible and infrared region previously.[15-18] A variety of mid- and far-infrared photodetectors have been reported based on 2D materials including black phosphorus,[19] black phosphorus arsenic,[20, 21] tellerium,[22] palladium diselenide,[23] platinum diselenide,[24] and graphene.[25] Recently, black phosphorus (bP) in particular has attracted significant attention, with zero bias internal quantum efficiencies >50% demonstrated at mid-wave infrared wavelengths.[26] This material exhibits a bulk bandgap of ~0.31 eV,[27] which can be increased by reducing layer thicknesses below ~8 layers,[28, 29] or decreased by alloying with As.[20] It also has strongly anisotropic optical and electrical properties which have been exploited, for example, in linear polarization detection.[29] Furthermore, several studies have shown that bP can be effectively combined with transition metal dichalcogenides (TMDCs) such as molybdenum disulfide (MoS_2),[30] tungsten diselenide,[31] and rhenium disulfide,[32] to form van der Waals heterojunction photodiodes. As such, bP has become a good model 2D material for MWIR detection, despite ongoing challenges surrounding its ambient degradation.[7, 26, 33] In this study, we explore the integration of bP/MoS_2 heterojunction photodiodes with Fabry-Pérot cavities, to form spectrally selective IR detectors. We demonstrate a simple detector architecture capable of attaining moderate room temperature detectivities with tunability within the mid- and short-wave infrared region (M/SWIR).

Results/Discussion

A conceptual diagram of the FP cavity enhanced bP/MoS_2 photodiode developed in this work is depicted in **Fig. 1c**. The asymmetric FP cavity under discussion is composed of an Au/Cr/AlO_x/bP/MoS_2/Cr/Au hybrid structure realized on a Si/SiO_2 holder substrate. The MoS_2 layer simultaneously acts as a MWIR transparent electron contact and the top dielectric of the FP cavity. Optical simulations of the absorption within the FP enhanced bP/MoS_2 heterojunction structure using different thicknesses of MoS_2 (10–150 nm) are shown in **Fig. 1d**. It can be clearly seen that by increasing the MoS_2 layer thickness, the resonant absorption peak position of the FP cavity redshifts (even with a constant 500 nm bottom cavity AlO_x thickness). Comparatively thin MoS_2 layers can be used to affect the resonance shift due to the higher MWIR refractive index of MoS_2 compared to that of the bottom AlO_x cavity. These devices were fabricated using a two-step mechanical exfoliation/dry transfer method to first assemble the bP/MoS_2 heterojunction structure then transfer it onto the Au/Cr/AlO_x bottom cavity.[26] The metal electrodes and top thin Cr/Au layer were defined by electron beam lithography and deposited by electron beam evaporation. In all cases a thin Cr "sticking" layer was found to be necessary to adhere Au to other layers in the stack. More details can be found in the Methods section and Supporting Information. Black phosphorus absorber thicknesses of 7–15 nm were used, which is thick enough to maintain its MWIR bulk bandgap of ~0.31 eV.[8, 9, 34] Optical micrographs of the fabrication procedure for the bP/MoS_2 heterojunction structure are provided in the Supporting Information. **Fig. 2a** shows the optical micrograph of a completed FP enhanced bP/MoS_2 photodiode. The overlapping regions between the bP, MoS_2 and thin Cr/Au mirror define the device area. To further explore the device structure, cross-sectional scanning transmission electron microscopy (STEM) high-angle annular dark-field imaging (HAADF) and energy-dispersive X-ray spectroscopy (EDX) of a FP enhanced bP/MoS_2 device are provided in the left and right panels of **Fig. 2b**, respectively. This pair of images shows clear continuous layers with some surface roughness. The device presented in **Fig. 2b** shows that the AlO_x layer (< 400 nm thick) exhibits some heterogeneity in the distribution of Al and O, giving rise to the HAADF contrast. This figure also shows the MoS_2 layer (~45 nm thick), the bP layer (~10 nm) and the top mirror (~15 nm thick). A HAADF image and accompanying EDX map of a zoomed-in area of AlO_x/bP/MoS_2 interfaces are shown in **Fig. 2c**. The layered nature of bP and MoS_2 can be clearly seen with monolayer spacings of 5.5 and 6.1 Å, respectively. Thin amorphous layers can be observed at bP/MoS_2 and bP/AlO_x interfaces as is commonly found on bP devices. In particular, the interface between the bP and AlO_x shows a region of intermixing, *i.e.* an AlP_xO_y layer. This intermediate layer, which is approximately 10 nm thick, is also evident in the accompanying EDX line scans and is believed to form during heated fabrication steps. Another HAADF micrograph and EDX map of a full FP enhanced bP/MoS_2 structure, including Cr mapping, is presented in the supporting information **Fig. S2**.

To characterize the ability of this structure to yield absorption (and thus responsivity) in narrow wavelength bands, the spectral photoresponses of fabricated photodiodes were characterized *via* an external detector port on a Fourier transform infrared (FTIR) spectrometer. All devices were measured at room temperature under zero bias with unpolarized light, unless otherwise indicated, and more details on measurement conditions are included in the Methods section. The normalized photoresponses of three representative photodiodes with similar rear AlO_x thickness but different MoS_2 thicknesses is shown in **Fig. 3a**. The peaks of the three bP/MoS_2 devices redshift as expected with increasing MoS_2 thickness, with peaks at 2.6 μm, 3.0 μm, and 3.3 μm corresponding to MoS_2 thicknesses of 12.3 nm, 36.7 nm, and 84.1 nm, respectively. This clearly confirms that the resonance of the FP cavity is controlling the spectral region of absorption for the bP/MoS_2 photodiodes.[11] We note that whilst the general trend and shape matches that expected from simulations, experimental devices were unable to replicate the narrow full-width-half-maximum (<300 nm) and peak position suggested by simulations. Explanations for this are provided in the supporting information. **Fig. 3b** and **3c** provide additional characterization results for the device of **Fig. 3a** with MoS_2 thickness 12.3 nm. This device has a spectral photoresponse with a full-width-half-maximum of ~420 nm. Its bias dependence is shown in **Fig. 3b**. The relative photoresponse, normalized to results at 0 V bias, is shown for devices under a forward bias of 0.1 V, and a reverse bias of -0.1 V, -0.5 V and -1 V with all other measurement conditions kept identical. As expected, the photoresponse clearly decreases under forward bias and increases under reverse bias. Similar to previous studies of bP based photodetectors, no significant change in photoresponse was found when cooling to 78

K, as shown in **Fig. 3c**, which compares the relative performance of the device at 298 K and 78 K.[35, 36] Under linearly polarised light, the FP enhanced bP/MoS_2 photodiodes also exhibited the expected polarisation angle dependence, as shown in supporting information **(Fig. S4b)**, with a polarisation ratio of 13:1 at 3 μm. Similar results were obtained using hexagonal boron nitride (hBN) and mica 2D layers for the top cavity, as shown in **Fig. S3** of the supporting information. The MoS_2-only cavity was ultimately favoured due to its comparitive simplicity which permitted consistently better experiemental results.

To provide an accompanying quantitative analysis of photodiode signal-to-noise performance, a set of additional measurements was taken. First, the light and dark *I-V* characteristics of a bP/MoS_2 photodiode were measured. **Fig. 4a** shows the dark *I-V* characteristics of a representative FP enhanced bP/MoS_2 photodiode at room temperature. The expected rectifying behavior of a narrow-bandgap material is clearly seen with a similar rectification ratio but a lower dark current compared to previous reports of bP/MoS_2 photodiodes of a similar design but with greater bP thickness,[26] which is likely a consequence of the reduced volume. The inset of **Fig. 4a** compares the measured *I-V* behavior with and without illumination from an ~1,200 K blackbody source. The generation of photocarriers causes the *I-V* curve to move downwards, resulting in an open-circuit voltage V_{oc} of 31.7 mV and a short-circuit current I_{sc} of 28.1 nA, thereby confirming that the device is working as a photodiode.

The relative photoresponse shown in **Fig. 3** can also be converted to an absolute current responsivity (A/W) by calibrating the FTIR system with a reference detector. As shown in the inset of **Fig. 4b**, a current responsivity above 0.1 A/W is demonstrated for a device operating at zero bias, corresponding to an external quantum efficiency η_e of ~5%, as shown in **Fig. S7**, which is relatively high among the 2D materials photodetectors with thin bP absorber (most of them are less than 2%),[37-43] but lower than those with thick bP absorber (which can reach as high as 35% with zero bias).[26] This η_e, combined with the zero bias resistance area product R_oA (extracted from the *I-V* measurement) taken on the same device, can be used to approximate the specific detectivity, as shown in **Fig. 4b**, according to ref.[6]:

$$D^* = \frac{\eta_e \lambda q}{hc}\left(\frac{4kT}{R_0 A}\right)^{-1/2}, \qquad (1)$$

where λ is the wavelength, *q* is the elementary charge, *c* is the speed of light in vacuum, T is the detector temperature, *h* is Planck's constant, and *k* is Boltzmann's constant. As shown in **Fig. 4b** a peak *D** of 1.7 × 10^9 cm $Hz^{1/2}$ W^{-1} at λ = 3.0 μm is found for the FP enhanced bP/MoS_2 photodiode. This value is lower than, but comparable to, existing demonstrations of high-performance room temperature MWIR photodiodes,[4, 22, 26, 44] a significant demonstration given the infancy of the optical design.

Linearity is another important aspect of photodetector performance. **Fig. 4c** shows a consistent linear relationship between the optical power density and photodiode short circuit current density J_{sc} when a representative photodiode (with a response in the SWIR) is illuminated with a pulsed λ = 1.55 μm laser diode source. The inset of **Fig. 4c** shows the individual measurements from which this plot was constructed depicting the device's on/off current under different illumination intensities.

A final set of characteristics explored in this study is the frequency response. **Fig. 5a** is obtained by subjecting a FP enhanced bP/MoS_2 photodiode, with a response in the SWIR, to pulsed illumination (λ = 1.55 μm) and shows that there is no observable baseline drift after successive pulses. **Fig. 5b** shows the rising and falling edge of a pulse with rise/fall times of 7.46 μs and 7.69 μs, respectively. These results were extracted at zero bias and the application of a reverse bias did not result in a measurable decrease in rise/fall time. **Fig. 5c** shows the measured frequency dependent photoresponse, with the 3-dB point at 50 kHz. The values of rise time (t_r) and bandwidth ($f_{3\text{-dB}}$) of the device are consistent with the $t_r = 0.35 / f_{3\text{-dB}}$ relationship.

Conclusions

In this study, we have demonstrated the effective integration of a bP/MoS_2 heterojunction photodiode into a Fabry-Pérot cavity to achieve spectrally-selective MWIR detection. The photoresponse peak position of these photodiodes can be altered by increasing the top dielectric thickness (in this case MoS_2), which redshifts the resonance of the FP cavity. At room temperature, under zero bias, the FP enhanced bP/MoS_2 device achieves specific detectivity and responsivity values of 1.7×10^9 cm $Hz^{1/2}$ W^{-1} and 0.11 A W^{-1} (at $\lambda = 3.0$ μm), respectively, as well as linearity and frequency response similar to state-of-the-art 2D MWIR detectors. These findings introduce an exciting class of Fabry-Pérot enhanced 2D detectors with the potential for tailored detection, useful in infrared spectroscopic applications.

Methods/Experimental

Device simulation

The optical absorption in the bP layer was simulated under normal incidence of a plane wave in the 1.5–4 μm wavelength range using a commercial software package (ANSYS Inc.) based on the finite difference time domain (FDTD) method. The illumination source was assumed to be linearly polarized along the armchair direction of the bP absorber. The frequency-dependent complex refractive indices of bP were taken from ref.[26, 45], those of MoS_2 and Cr were taken from ref. [46, 47], and those of AlO_x and Au were taken from ref.[48, 49].

Device fabrication

A detailed description of device fabrication is given with accompanying images in the supporting information (**Fig. S1c**–**f**). Briefly, mechanically exfoliated bP and MoS_2 flakes were transferred onto an Au/Cr/AlO_x substrate using a polymethyl methacrylate (PMMA) dry transfer process. The Au, AlO_x and Cr layers were all deposited *via* electron beam evaporation onto a Si/SiO_2 holder chip. The stoichiometry of the AlO_x layer was improved by annealing in air. Transmission properties of the AlO_x layer are provided in supporting information (**Fig. S1a** and **S1b)**. The top cavity metal and contact regions were defined using two separate electron beam lithography steps and in both cases the Cr/Au contacts were deposited using electron beam evaporation. The thickness of the bP and MoS_2 flakes were first measured by atomic force microscopy (AFM, Cypher ES from Asylum Research, US). Note that due to the known stability issues of bP, initial AFM measurements were used to construct a color-to-thickness map which was used for the remainder of the study.

A 100-nm-thick lamella was prepared using the focused ion beam (FIB) lift-out method in a FIB/scanning electron microscope (Zeiss NVision 40). The sample was thinned down with a gallium beam of 30 kV before performing the final steps at 5 kV to reduce beam damage. The lamella was analyzed in a double Cs-corrected TITAN Themis transmission electron microscope (Thermo Fisher Scientific). The microscope was operated in the scanning TEM (STEM) mode at 200 kV with a beam current of 200 pA. A multi-polynomial background was subtracted from the energy-dispersive X-ray spectra using the software Velox (Thermo Fisher Scientific) to extract the net intensity of each edge of interest.

Device characterization

The spectral photoresponses of fabricated photodiodes were measured using a custom-built IR characterization platform at the external detector port of a FTIR spectrometer (Perkin Elmer Frontier). The sample photoresponse, under illumination from a modulated 1,200 K FTIR blackbody source, was amplified (SRS570) and fed back into the FTIR to extract a spectrum. The influence of the blackbody's wavelength dependence (as measured using an internal Deuterated triglycine sulfate detector) was corrected in all cases. For **Fig. 3b**, biases were applied using the abovementioned pre-amplifier and low temperature measurements were performed in a liquid nitrogen cooled cryostat with a MWIR transmissive window. For measurements in **Fig. 4b**, the set-up was calibrated using a NIST traceable Ge photodiode illuminated under identical conditions.

Current-voltage measurements were taken in a two-probe configuration (Keithley 2450) with and without ~1200 K blackbody illumination. Pulsed measurements were performed using a 1.55 μm laser diode illumination source with the detector held at room temperature under zero bias. Linearity and frequency response characterization was performed by alternating the laser intensity and modulation respectively. A NIST traceable Ge photodiode was also used to calibrate the setup for **Fig. 4c**.

ASSOCIATED CONTENT

Supporting Information

The Supporting Information is available free of charge at

Details of methods; transmission of AlO_x before and after annealing at 400 °C; optical and TEM images, and polarization dependence of Fabry-Pérot cavity enhanced bP/MoS_2 photodiodes; characterization of hBN and mica based Fabry-Pérot cavity photodetectors (PDF)

AUTHOR INFORMATION

Corresponding Author:

*E-mail: james.bullock@unimelb.edu.au

ORCID:

Wei Yan: 0000-0002-0523-4805

Vivek Raj Shresha: 0000-0002-7731-7677

Quentin Jeangros: 0000-0003-2885-975X

Nima Sefidmooye Azar: 0000-0002-3263-7044

Sivacarendran Balendhran: 0000-0002-4390-3491

Christophe Ballif: 0000-0001-8989-0545

Kenneth Crozier: 0000-0003-0947-001X

James Bullock: 0000-0001-7903-9642

Author Contributions

W.Y. and J.B. conceived the project and designed the experiments. W.Y., N.S., and S.B. fabricated devices. V.R.S. and K.C. assisted with optical design and device simulations. Q.J. and C.B. performed TEM measurements. W.Y. and J.B. performed optical measurements, analysed the data and wrote the manuscript. All authors commented on the manuscript.

Acknowledgements

This work was supported by the Defense Advanced Research Projects Agency (HR0011-16-1-0004) and by the Australian Research Council (DP180104141). Work was performed in part at the Melbourne Centre for Nanofabrication (MCN) in the Victorian Node of the Australian National Fabrication Facility (ANFF) and at the Melbourne Characterization and Fabrication Platform (MCFP). Q.J. and C.B. were supported from the Swiss National Science Foundation (SNF), Switzerland, under grants no. 200021L_172924/1 and CRSII5_171000.

References

1. Xia, F.; Wang, H.; Xiao, D.; Dubey, M.; Ramasubramaniam, A., Two-Dimensional Material Nanophotonics. *Nat. Photon.* **2014,** *8*, 899-907.
2. Jakšić, Z., *Micro and Nanophotonics for Semiconductor Infrared Detectors*. Springer: 2014; *1*, p 1-42.
3. Na, J.; Lee, Y. T.; Lim, J. A.; Hwang, D. K.; Kim, G.-T.; Choi, W. K.; Song, Y.-W., Few-Layer Black Phosphorus Field-Effect Transistors with Reduced Current Fluctuation. *ACS Nano* **2014,** *8*, 11753-11762.
4. Rogalski, A., Hgcdte Infrared Detector Material: History, Status and Outlook. *Rep. Prog. Phys.* **2005,** *68*, 2267-2336.
5. Piotrowski, J.; Gawron, W., Extension of Longwavelength Ir Photovoltaic Detector Operation to near Room-Temperatures. *Infrared Phys. Techn.* **1995,** *36*, 1045-1051.
6. Rogalski, A.; Adamiec, K.; Rutkowski, J., *Narrow-Gap Semiconductor Photodiodes*. SPIE Press: 2000; *77*, p 237-375.
7. Xia, F.; Wang, H.; Jia, Y., Rediscovering Black Phosphorus as an Anisotropic Layered Material for Optoelectronics and Electronics. *Nat. Commun.* **2014,** *5*, 4458.
8. Yuan, H.; Liu, X.; Afshinmanesh, F.; Li, W.; Xu, G.; Sun, J.; Lian, B.; Curto, A. G.; Ye, G.; Hikita, Y.; Shen, Z.; Zhang, S.-C.; Chen, X.; Brongersma, M.; Hwang, H. Y.; Cui, Y., Polarization-Sensitive Broadband Photodetector Using a Black Phosphorus Vertical P–N Junction. *Nat. Nanotechn.* **2015,** *10*, 707-713.

9. Ling, X.; Wang, H.; Huang, S.; Xia, F.; Dresselhaus, M. S., The Renaissance of Black Phosphorus. *PNAS* **2015,** *112*, 4523.

10. Azar, N. S.; Shrestha, V. R.; Crozier, K. B., Bull's Eye Grating Integrated with Optical Nanoantennas for Plasmonic Enhancement of Graphene Long-Wave Infrared Photodetectors. *Appl. Phys. Lett.* **2019,** *114*, 091108.

11. Huang, X.; Feng, X.; Chen, L.; Wang, L.; Tan, W. C.; Huang, L.; Ang, K.-W., Fabry-Perot Cavity Enhanced Light-Matter Interactions in Two-Dimensional Van Der Waals Heterostructure. *Nano Energy* **2019,** *62*, 667-673.

12. Liang, W.; Bockrath, M.; Bozovic, D.; Hafner, J. H.; Tinkham, M.; Park, H., Fabry - Perot Interference in a Nanotube Electron Waveguide. *Nature* **2001,** *411*, 665-669.

13. Wang, Q.; Guo, J.; Ding, Z.; Qi, D.; Jiang, J.; Wang, Z.; Chen, W.; Xiang, Y.; Zhang, W.; Wee, A. T. S., Fabry–Perot Cavity-Enhanced Optical Absorption in Ultrasensitive Tunable Photodiodes Based on Hybrid 2d Materials. *Nano Lett.* **2017,** *17*, 7593-7598.

14. Lochbaum, A.; Fedoryshyn, Y.; Dorodnyy, A.; Koch, U.; Hafner, C.; Leuthold, J., On-Chip Narrowband Thermal Emitter for Mid-Ir Optical Gas Sensing. *ACS Photonics* **2017,** *4*, 1371-1380.

15. Guo, Y.; Jiang, S.; Chen, X.; Mattei, M.; Dieringer, J. A.; Ciraldo, J. P.; Van Duyne, R. P., Using a Fabry–Perot Cavity to Augment the Enhancement Factor for Surface-Enhanced Raman Spectroscopy and Tip-Enhanced Raman Spectroscopy. *J. Phys. Chem. C* **2018,** *122*, 14865-14871.

16. Shu, S.; Li, Z.; Li, Y. Y., Triple-Layer Fabry-Perot Absorber with near-Perfect Absorption in Visible and near-Infrared Regime. *Opt. Express* **2013,** *21*, 25307-25315.

17. Li, Q.; Lu, J.; Gupta, P.; Qiu, M., Engineering Optical Absorption in Graphene and Other 2d Materials: Advances and Applications. *Adv. Opt. Mater.* **2019,** *7*, 1900595.

18. Lee, I.-H.; Yoo, D.; Avouris, P.; Low, T.; Oh, S.-H., Graphene Acoustic Plasmon Resonator for Ultrasensitive Infrared Spectroscopy. *Nat. Nanotechn.* **2019,** *14*, 313-319.

19. Guo, Q.; Pospischil, A.; Bhuiyan, M.; Jiang, H.; Tian, H.; Farmer, D.; Deng, B.; Li, C.; Han, S.-J.; Wang, H.; Xia, Q.; Ma, T.-P.; Mueller, T.; Xia, F., Black Phosphorus Mid-Infrared Photodetectors with High Gain. *Nano Lett.* **2016,** *16*, 4648-4655.

20. Amani, M.; Regan, E.; Bullock, J.; Ahn, G. H.; Javey, A., Mid-Wave Infrared Photoconductors Based on Black Phosphorus-Arsenic Alloys. *ACS Nano* **2017,** *11*, 11724-11731.

21. Long, M.; Gao, A.; Wang, P.; Xia, H.; Ott, C.; Pan, C.; Fu, Y.; Liu, E.; Chen, X.; Lu, W.; Nilges, T.; Xu, J.; Wang, X.; Hu, W.; Miao, F., Room Temperature High-Detectivity Mid-Infrared Photodetectors Based on Black Arsenic Phosphorus. *Sci. Adv.* **2017,** *3*, e1700589.

22. Amani, M.; Tan, C.; Zhang, G.; Zhao, C.; Bullock, J.; Song, X.; Kim, H.; Shrestha, V. R.; Gao, Y.; Crozier, K. B.; Scott, M.; Javey, A., Solution-Synthesized High-Mobility Tellurium Nanoflakes for Short-Wave Infrared Photodetectors. *ACS Nano* **2018,** *12*, 7253-7263.

23. Zeng, L. H.; Wu, D.; Lin, S. H.; Xie, C.; Yuan, H. Y.; Lu, W.; Lau, S. P.; Chai, Y.; Luo, L. B.; Li, Z. J.; Tsang, Y. H., Controlled Synthesis of 2d Palladium Diselenide for Sensitive Photodetector Applications. *Adv. Funct. Mater.* **2019,** *29*, 9.

24. Mak, K. F.; Lee, C.; Hone, J.; Shan, J.; Heinz, T. F., Atomically Thinmos2: A New Direct-Gap Semiconductor. *Phys. Rev. Lett.* **2010,** *105*.

25. Wang, X.; Cheng, Z.; Xu, K.; Tsang, H. K.; Xu, J.-B., High-Responsivity Graphene/Silicon-Heterostructure Waveguide Photodetectors. *Nat. Photon.* **2013,** *7*, 888-891.

26. Bullock, J.; Amani, M.; Cho, J.; Chen, Y.-Z.; Ahn, G. H.; Adinolfi, V.; Shrestha, V. R.; Gao, Y.; Crozier, K. B.; Chueh, Y.-L.; Javey, A., Polarization-Resolved Black Phosphorus/Molybdenum Disulfide Mid-Wave Infrared Photodiodes with High Detectivity at Room Temperature. *Nat. Photon.* **2018,** *12*, 601-607.

27. Morita, A., Semiconducting Black Phosphorus. *Appl. Phys. A* **1986,** *39*, 227-242.

28. Tran, V.; Soklaski, R.; Liang, Y.; Yang, L., Layer-Controlled Band Gap and Anisotropic Excitons in Few-Layer Black Phosphorus. *Phys. Rev. B* **2014,** *89*, 235319.

29. Qiao, J.; Kong, X.; Hu, Z.-X.; Yang, F.; Ji, W., High-Mobility Transport Anisotropy and Linear Dichroism in Few-Layer Black Phosphorus. *Nat. Commun.* **2014,** *5*.

30. Deng, Y.; Luo, Z.; Conrad, N. J.; Liu, H.; Gong, Y.; Najmaei, S.; Ajayan, P. M.; Lou, J.; Xu, X.; Ye, P. D., Black Phosphorus–Monolayer Mos2 Van Der Waals Heterojunction P–N Diode. *ACS Nano* **2014,** *8*, 8292-8299.

31. Chen, P.; Zhang, T. T.; zhang, J.; Xiang, J.; Yu, H.; Wu, S.; Lu, X.; Wang, G.; Wen, F.; Liu, Z.; Yang, R.; Shi, D.; Zhang, G., Gate Tunable Wse2–Bp Van Der Waals Heterojunction Devices. *Nanoscale* **2016,** *8*, 3254-3258.

32. Shim, J.; Oh, S.; Kang, D.-H.; Jo, S.-H.; Ali, M. H.; Choi, W.-Y.; Heo, K.; Jeon, J.; Lee, S.; Kim, M.; Song, Y. J.; Park, J.-H., Phosphorene/Rhenium Disulfide Heterojunction-Based Negative Differential Resistance Device for Multi-Valued Logic. *Nat. Commun.* **2016,** *7*, 13413.

33. Huang, M.; Wang, M.; Chen, C.; Ma, Z.; Li, X.; Han, J.; Wu, Y., Broadband Black-Phosphorus Photodetectors with High Responsivity. *Adv. Mater.* **2016,** *28*, 3481-3485.

34. Liu, H.; Neal, A. T.; Zhu, Z.; Luo, Z.; Xu, X.; Tománek, D.; Ye, P. D., Phosphorene: An Unexplored 2d Semiconductor with a High Hole Mobility. *ACS Nano* **2014,** *8*, 4033-4041.

35. Villegas, C. E. P.; Rocha, A. R.; Marini, A., Anomalous Temperature Dependence of the Band Gap in Black Phosphorus. *Nano Lett.* **2016,** *16*, 5095-5101.

36. Villegas, C. E. P.; Rodin, A. S.; Carvalho, A.; Rocha, A. R., Two-Dimensional Exciton Properties in Monolayer Semiconducting Phosphorus Allotropes. *Phys. Chem. Chem. Phys.* **2016,** *18*, 27829-27836.

37. Deckoff-Jones, S.; Lin, H.; Kita, D.; Zheng, H.; Li, D.; Zhang, W.; Hu, J., Chalcogenide Glass Waveguide-Integrated Black Phosphorus Mid-Infrared Photodetectors. *Journal of Optics* **2018,** *20*, 044004.

38. Buscema, M.; Groenendijk, D. J.; Blanter, S. I.; Steele, G. A.; van der Zant, H. S. J.; Castellanos-Gomez, A., Fast and Broadband Photoresponse of Few-Layer Black Phosphorus Field-Effect Transistors. *Nano Letters* **2014,** *14*, 3347-3352.

39. Liu, Y.; Cai, Y.; Zhang, G.; Zhang, Y.-W.; Ang, K.-W., Al-Doped Black Phosphorus P-N Homojunction Diode for High Performance Photovoltaic. *Adv. Funct. Mater.* **2017,** *27*, 1604638.

40. Zheng, Y.; Hu, Z.; Han, C.; Guo, R.; Xiang, D.; Lei, B.; Wang, Y.; He, J.; Lai, M.; Chen, W., Black Phosphorus Inverter Devices Enabled by in-Situ Aluminum Surface Modification. *Nano Research* **2019,** *12*, 531-536.

41. Gong, F.; Wu, F.; Long, M.; Chen, F.; Su, M.; Yang, Z.; Shi, J., Black Phosphorus Infrared Photodetectors with Fast Response and High Photoresponsivity. *Rapid Research Letters* **2018,** *12*, 1800310.

42. Xu, M.; Gu, Y.; Peng, R.; Youngblood, N.; Li, M., Black Phosphorus Mid-Infrared Photodetectors. *Applied Physics B* **2017,** *123*.

43. Miao, J.; Song, B.; Xu, Z.; Cai, L.; Zhang, S.; Dong, L.; Wang, C., Single Pixel Black Phosphorus Photodetector for near-Infrared Imaging. *Small* **2018,** *14*, 1702082.

44. Martyniuk, P.; Kopytko, M.; Rogalski, A., Barrier Infrared Detectors. *Opto-Electron. Rev.* **2014,** *22*, 127-146.

45. Mao, N.; Tang, J.; Xie, L.; Wu, J.; Han, B.; Lin, J.; Deng, S.; Ji, W.; Xu, H.; Liu, K.; Tong, L.; Zhang, J., Optical Anisotropy of Black Phosphorus in the Visible Regime. *J. Am. Chem. Soc.* **2016,** *138*, 300-305.

46. Ermolaev, G. A.; Yakubovsky, D. I.; Stebunov, Y. V.; Arsenin, A. V.; Volkov, V. S., Spectral Ellipsometry of Monolayer Transition Metal Dichalcogenides: Analysis of Excitonic Peaks in Dispersion. *J. Vac. Sca. Technol. B* **2020,** *38*, 014002.

47. Johnson, P. B.; Christy, R. W., Optical Constants of Transition Metals: Ti, V, Cr, Mn, Fe, Co, Ni, and Pd. *Phys. Rev. B* **1974,** *9*, 5056-5070.
48. Palik, E. D., *Handbook of Optical Constants of Solids*. Academic press: 1998; *3*, p 653-682.
49. Rosenblatt, G.; Simkhovich, B.; Bartal, G.; Orenstein, M., Nonmodal Plasmonics: Controlling the Forced Optical Response of Nanostructures. *Phys. Rev. X* **2020,** *10*, 011071.

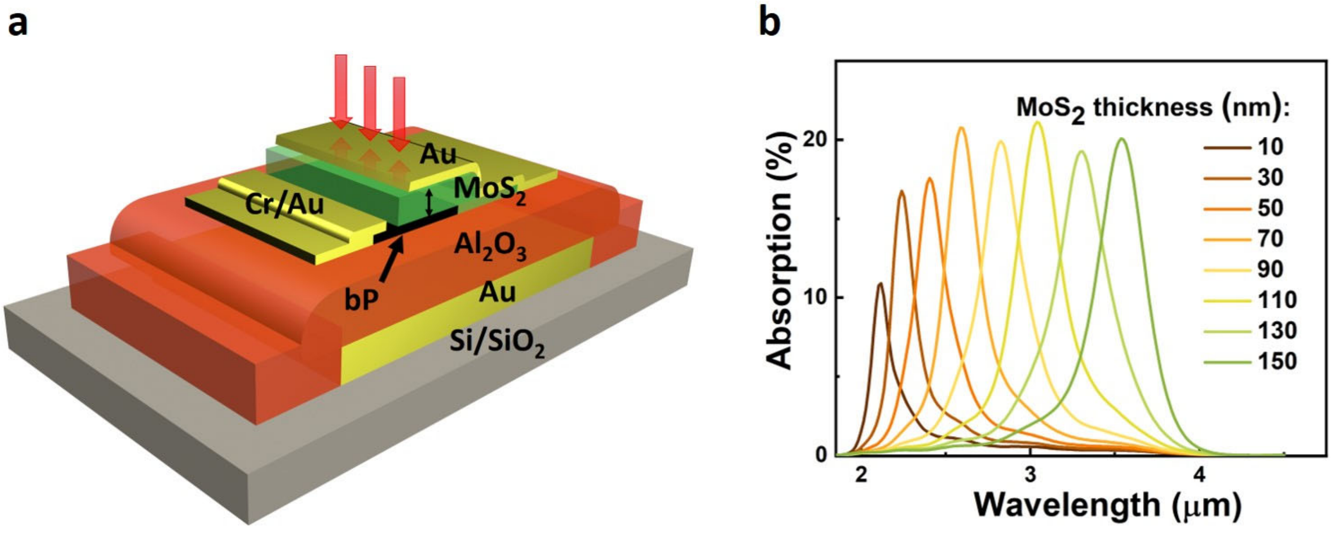

Figure 1. Fabry-Pérot enhanced bP/MoS_2 heterojunction photodiode concept. a, Schematic of Fabry-Pérot enhanced bP/MoS_2 photodiode developed in this work, showing the heterojunction and contact configuration. **b**, Simulated absorption in bP layer of the Fabry-Pérot enhanced bP/MoS_2 photodiode developed in this work (see Fig. 1c) with different MoS_2 top dielectric thicknesses (10–150 nm). Absorber (bP) = 15 nm, front mirror (Cr/Au) = 1/15 nm, rear mirror (Cr/Au) = 1/100 nm, rear dielectric (AlO_x) = 500 nm. References to refractive index values given in the Methods section.

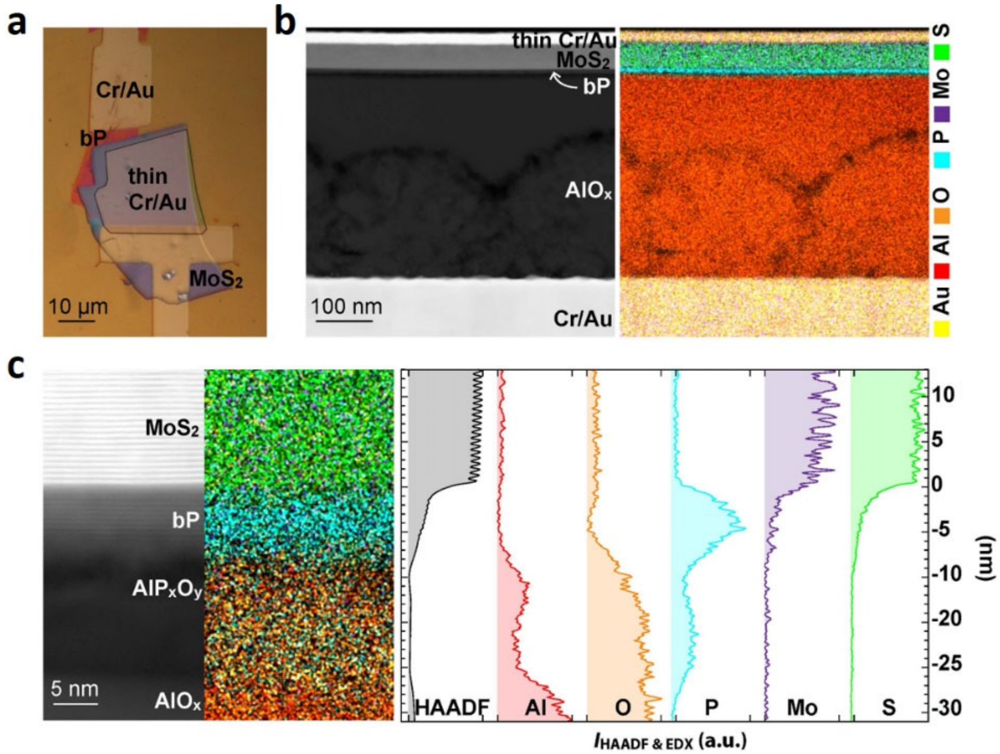

Figure 2. Fabry-Pérot bP/MoS$_2$ heterojunction photodiode structure. a, Optical micrograph of a completed bP/MoS$_2$ heterojunction device. **b**, Cross-sectional STEM HAADF (left) image and corresponding EDX (right) map of a full FP enhanced bP/MoS$_2$ device structure showing all layers. **c**, STEM HAADF (left) and EDX (middle) mapping images of the MoS$_2$/bP/AlO$_x$ interfaces of the same device. The right panel shows the HAADF line profile alongside the net EDX intensity of the Al, O, P, Mo, and S *K* edges after background subtraction.

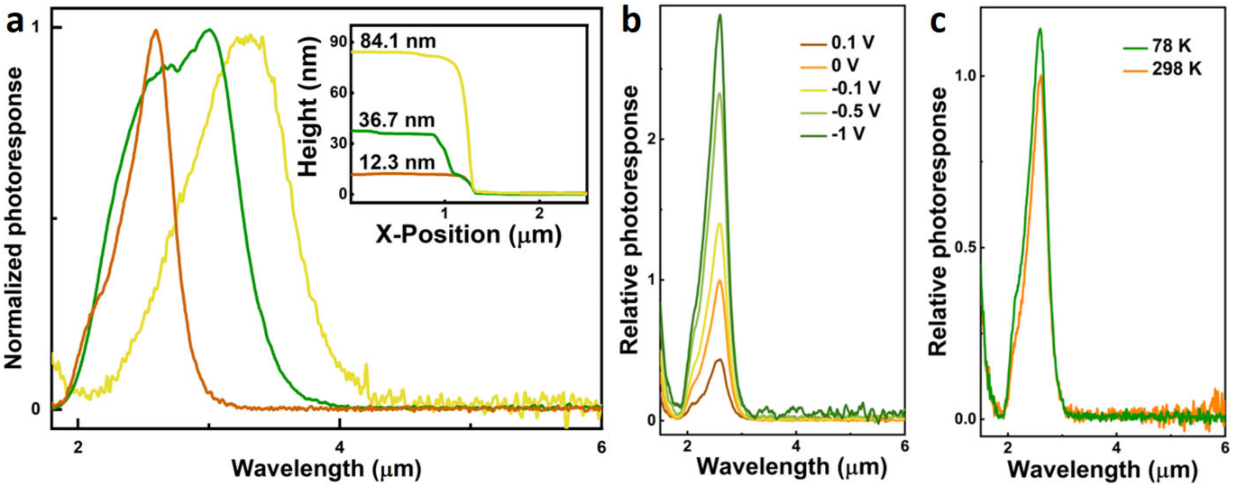

Figure 3. Photoresponse. **a**, Spectral shift of bP/MoS$_2$ devices with different MoS$_2$ thicknesses, 12.3 nm, 36.7 nm, and 84.1 nm. **b**, Bias dependence of bP/MoS$_2$ device measured at 0.1 V, 0 V, -0.1 V, -0.5 V, and -1 V, showing the effect of biasing on the device performance. **c**, Temperature dependence of bP/MoS$_2$ device measured at 78 K and 298 K.

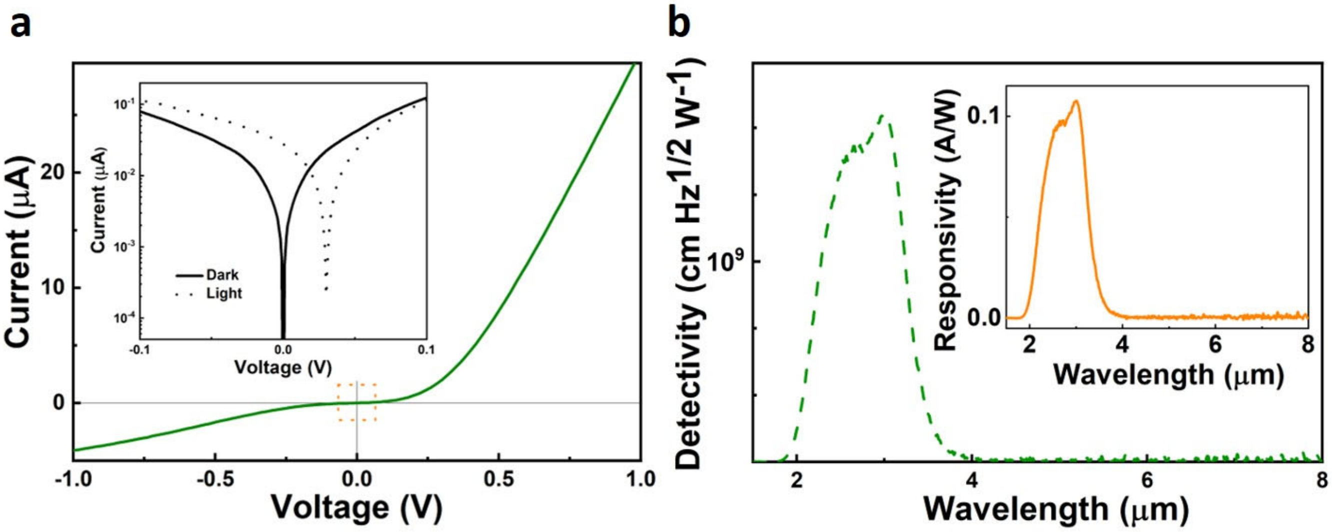

Figure 4. Performance of the bP/MoS$_2$ photodiode at room temperature with a bias of 0 V. a, *I-V* curve of bP/MoS$_2$ heterojunction photodiode. Inset: magnified measurement taken in the dark and light under illumination by a ~1,200 K blackbody source. **b**, Specific detectivity for a FP enhanced bP/MoS$_2$ heterojunction at room temperature. Inset: current responsivity of the same device.

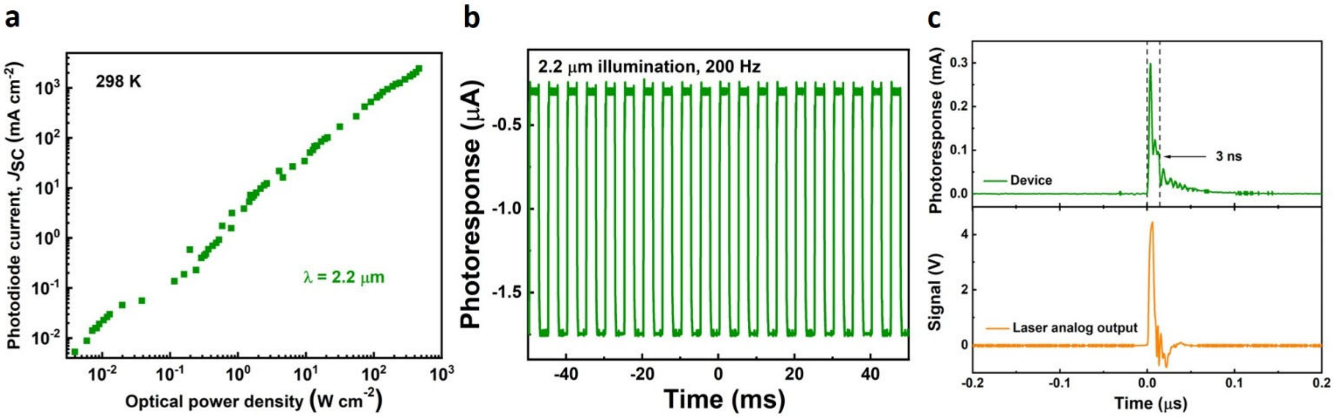

Figure 5. Frequency response. a, Linearity measurement, showing consistent proportionality between the optical power density and the photodiode current density for a FP enhanced bP/MoS_2 photodiode with a SWIR response. Excitation is performed with a λ = 2.2 μm at a frequency of 200 Hz. **b**, Response of a FP enhanced bP/MoS_2 photodiode under a modulated illumination showing no observable baseline shift. **c**, Response time of a FP enhanced bP/MoS_2 device. All characterization performed using a λ = 2.2 μm modulated laser diode.